Numerical estimation of the bearing capacity of resistance spot welds in martensitic boron steels using a J-integral fracture criterion

D. Dorribo[a,b], L. Greve[c], P. Díez[a], I. Arias[a,d], X. Larráyoz-Izcara[b,d]

[a]Laboratori de Càlcul Numèric, Department of Civil and Environmental Engineering,
Universitat Politècnica de Catalunya, BarcelonaTech, Barcelona 08034, Spain
[b]SEAT S.A. Autovía A-2, km 85, Martorell 08760, Spain
[c]Volkswagen AG, Group Research, P.O. Box 1777, Wolfsburg 38436, Germany
[d]co-corresponding authors

Abstract

Predicting the bearing capacity of resistance spot welds (RSW) during vehicle crash tests has become a crucial task for the automotive industry, since the recent introduction of advanced high strength steels (AHSS) such as martensitic boron steels (e.g. 22MnB5). The spot weld joints of these steels exhibit relatively low bearing strengths, compared to those of more ductile high strength steels. Currently, the bearing capacity of spot weld joints is characterized through extensive experimental campaigns. In this article, a model for quantification of the bearing capacity of RSW using a finite-element J-integral fracture criterion is presented. The model takes into account geometric and mechanical features of the spot weld, namely the weld diameter and the mechanical properties distribution resulting from the welding process. An experimental loading test campaign is carried out for calibration and validation purposes, considering multiple sheet thickness combinations, loading angles and weld sizes. Experimental observations of the failed spot welds and preliminary simulations show that failure is caused mostly by stress concentration around the sharp weld notch. Consequently, the J-integral obtained from detailed finite element simulations is used to asses the stress/strain concentration along the first crack advance direction predicted by the acoustic tensor. The computed J-integral values are compared to the material toughness to obtain the joint's maximum force. The resulting simulated and experimental bearing capacities show a good agreement for all tested configurations.

1. Introduction

The increasingly demanding requirements on fuel consumptions and emissions in the automotive industry are a challenge for the development of current and future vehicle projects. For this purpose, advanced high strength steels (AHSS) have been introduced to a large extent in recent years to reduce the total weight of new generation car body structures while maintaining or even improving their crashworthiness [1, 2]. Martensitic boron steels (e.g. 22MnB5), belonging to this type of steels, provide a significant improvement in the sheet structural crash performance. The bearing capacity of the joints between AHSS crash-relevant components becomes now critical, specially in the case of the widely applied resistance spot weld (RSW) technology.

During the development of new car projects, finite element full-vehicle models are used to predict the crash behavior. To alleviate the computational cost, full-vehicle simulations use shell elements for the sheets and simplified spring-beam models for the joints with simple load-based failure criteria. In conventional ductile steels, the higher strength of the martensitic welded zone as compared to the surrounding ductile steel results in most failures occurring in the sheets rather than at the joints. For this reason, these simplified methodologies were able to provide reasonable predictions for standard ductile steels, without precise quantitative knowledge of the bearing capacity of the joints. However, with the introduction of AHSS, these models need to be extended to reproduce the new observed weld failure mechanisms such as failure of the spot weld fusion zone [3–5]. The bearing forces at the joints became a critical parameter of the model, and are currently obtained from extensive and expensive experimental characterization campaigns. This procedure presents several limitations, since the extrapolation of maximum force values to different conditions as those tested during the experimental characterization campaign is not precise. Furthermore, although presenting a good first approximation of the failure response of the spot weld during full-vehicle crash simulations, the simplified models are not accurate enough for optimal vehicle structure development. The objective of this work is twofold: (1) to develop a model that is able to partially replace the extensive experimental campaign in providing parameters for the crash simulation simplified

2

models, and (2) to gain understanding of spot weld joints failure in order to improve current simplified models that are incorporated in full-vehicle crash simulations with thousands of spot welds.

Failure of RSWs is in general a complex process mainly due to the heterogeneity of the resulting material in the vicinity of the joint after the welding process. Generally, three different material zones can be distinguished near a spot weld, namely, towards the geometrical center:(i) the base material (BM), (ii) the heat-affected zone (HAZ), and (iii) the fusion zone (FZ) or nugget. The FZ is the result of the melting process during welding and ensures the joining of the sheets. In the case of martensitic steels, both FZ and BM consist of a fully martensitic microstructure and exhibit high strength values while the in–between HAZ contains different hardening grades ranging from low to high strength values [6]. A cross section of a RSW with the different weld zones is shown in Fig. 1. In addition, the welding process is difficult to control: the resulting geometrical features, such as the weld notch morphology, the accurate nugget diameter, and the presence of imperfections, inclusions or porosities, all having a strong influence on the joint's bearing capacity, cannot be predicted.
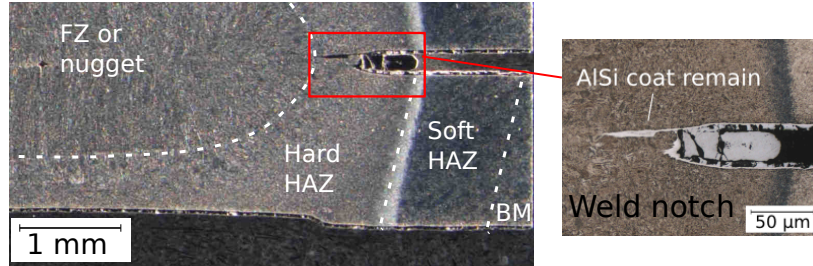

Figure 1: Scheme of the 22MnB5 spot weld zones. On the right, zoom of the irregular weld notch.

For all these reasons, multiple and complex fracture modes may occur in spot welds (see Fig. 2), depending on the weld geometry, namely the weld size and the sheets thickness combination, the chemical composition of the joined materials, and the loading conditions.

Based on the complex property distribution, geometrical uncertainties, and the diversity of failure modes, accurate modeling of spot weld fracture is challenging. Attempts to model spot weld failure have been made for a long time. In the first approaches, the heterogeneities of spot welds mate-

3

BPO - BM   FIF   TDF

BPO - SHAZ   PIF   PDF

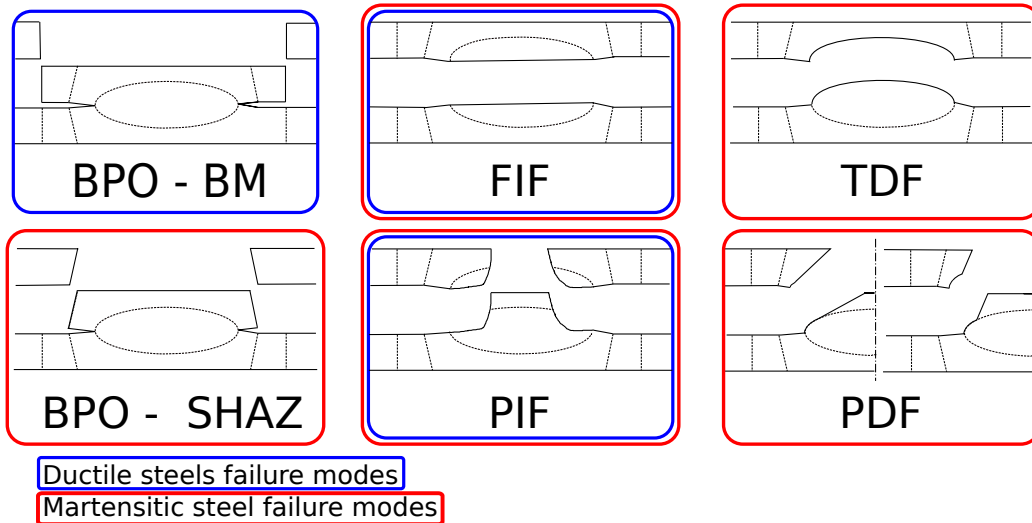Ductile steels failure modes
Martensitic steel failure modes

Figure 2: Most common failure modes regarding the external appearance of the failed spot welds [7, 8]. The typical failure modes for RSWs in conventional ductile steels are (i) button pull-out in BM (BPO-BM); and (i) full or partial interface failure (FIF / PIF) [7, 9–12]. Button pull-out (BPO) refers to sheet failure around the spot weld and partial or full interface failure (PIF/FIF) indicates nugget split into two parts. In joints of martensitic steels, the aforementioned inhomogeneous material properties distribution introduces new failure mechanisms: (i) failure due to necking in the softened heat-affected zone (SHAZ) leading to BPO failure mode appearance (BPO-SHAZ), and (ii) failure mechanism along the nugget and HAZ boundary due to ductile shear. In some conditions, the latter leads to a new failure mode in 22MnB5 joints called Partial Dome Failure (PDF) or Total Dome Failure (TDF).[3, 8, 13, 14].

rial properties were not considered and the maximum forces were calculated from analytical formulas [15–18]. In these works, BPO-BM failure is predicted assuming the weld to be a rigid cylinder and evaluating the plastic collapse of the surrounding sheet upon loading. In the case of FIF, the maximum forces are calculated using linear elastic fracture mechanics [19], i.e. relating stress intensity factors at the weld notch with the applied forces and comparing the values with the critical material toughness. However, these simplified approaches fail for martensitic steels (such as press hardened martensitic boron steels or cold rolled martensitic steels) joints because, in contrast to other conventional automotive steels, the sheet material in these RSWs have comparable strength to the weld material [7, 13, 14], and consequently, the fusion zone cannot be considered neither rigid nor completely elastic anymore.

4

Consequently, more detailed finite element models have been introduced to predict RSW fracture. Some authors focused on detailed models of the plastic and fracture response of the multiple spot weld material zones [20–22]. Strain-based fracture models using a detailed description of void coalescence, nucleation and growth during loading have also been used [23, 24]. While giving reasonable results for some fracture mechanisms, this kind of models fail to accurately capture the fracture by cleavage crack propagation originating from the weld notch, which is controlled by the FZ fracture toughness, since fine meshes - unaffordable for industrial applications - are needed to resolve the strain fields in the vicinity of the notch (see Fig. 3). Therefore, a fracture mechanics approach should be used for failure predictions of spot welds in martensitic steels [14]. Furthermore, extensive, large experimental campaigns are needed to determine the numerous parameters of these complex strain-based fracture models.
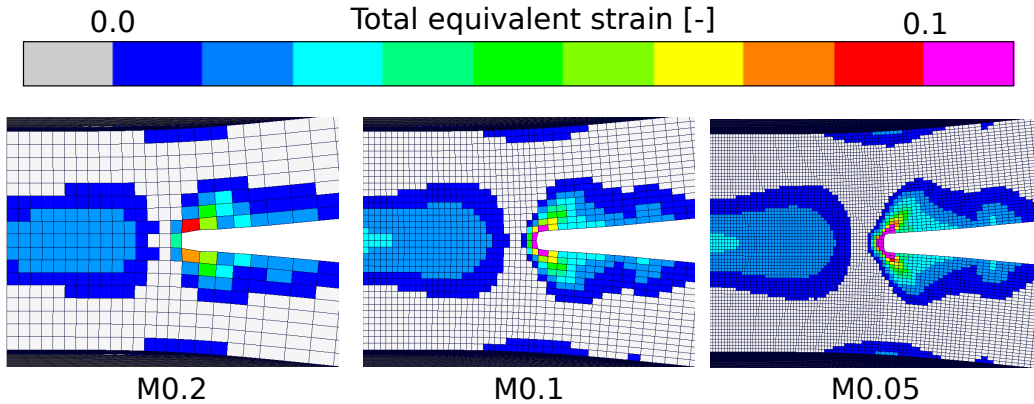

Figure 3: Results of plastic strain concentration around the weld notch in a normal tests simulation of a martensitic steel spot weld. M0.2, M0.1 and M0.05 indicate 0.2 mm, 0.1 mm and 0.05 mm mesh sizes, respectively.

To overcome these difficulties, a fracture criterion based on the J-integral has been recently proposed. The J-integral is used to evaluate the stress concentration around the weld notch and compared with a critical value, a material parameter [3–5]. Since the fracture criterion is not based on the plastic strain, the cumbersome and extensive calibration of the plastic models is avoided, rendering this method very attractive for industry. Although yielding promising results, the models reported so far are not predictive, since they require certain *a priori* information about the particular fracture mechanism. Apart from that, previous model haven't been tested for multiple

thickness combinations, weld diameters and mixed-modes.

In this work, the validity of the J-integral fracture criterion for the prediction of failure of spot welds in martensitic boron steel 22MnB5 sheets is examined. In order to improve the predictive ability of the resulting model, a criterion to locally determine the fracture mode based on the acoustic tensor is incorporated. An experimental and simulation campaign is designed, for quantitative validation purposes considering multiple spot weld diameters, loading angles and combinations of sheet thicknesses.

The validation program is presented in Section 2. It includes a detailed description of the finite element (FE) spot weld model in Section 2.1, and the methodology of the experimental campaign used for calibration and validation in Section 2.2. All results are presented in Section 3, including an analysis of the microstructure and the geometry of the joints that is necessary for setting up the FE model in Section 3.1. The experimental force-displacement curves of loaded joints are presented in Section 3.2, and the analysis of the fracture of the failed spot welds in Section 3.3. Simulated and experimental results are compared in Section 3.4 using the force-displacement curves and in Section 3.5 using the obtained maximum forces. Finally, some conclusions are presented in Section 4.

2. Validation program

An extensive both experimental and simulation test campaign is designed for quantitative validation purposes. The test matrix focuses on the three main variables controlling the joint fracture response, namely (i) welded sheet thickness, (ii) the applied loading angle, and (iii) the spot weld size. Other important variables such as the loading velocity, the presence of residual stresses, or the sheet's coating material and thickness have been neglected in the present work. The joint's bearing capacity has been chosen as the main output for validation. The full force-displacement curves have also been compared in a qualitative manner.

2.1. Finite Element estimation of spot weld bearing capacity

The FE spot weld models used for the prediction of joints's bearing capacity includes the main weld geometrical features as well as the material heterogeneities of these types of joints. Simulations are performed in this test using the explicit dynamic finite element method (FEM) code, Virtual

6

Performance Solution (VPS), also known in industry as PAMCRASH. The code has been adapted to perform quasistatic simulations.

A complex embedded fracture model such as [25] is not desirable due to the high computational costs not suited for the industrial purpose of this work. Besides, the fracture criteria must therefore be simple and robust in order to be able to reproduce all loading and geometrical alternatives of the weld joints without large experimental calibration.

2.1.1. Mesh and constitutive model

The computational mesh is shown in Fig. 4. The weld nugget is assumed to be cylindrical, and its diameter is obtained from measurements in the cross-sectioned weld samples presented and explained in Section 3.1. Solidification voids in the fusion zone and the accurate geometry of the electrode indentation are neglected in the geometry definition of the spot weld. Moreover, the weld notch is considered regular and acute in contrast to the actual geometry that is strongly irregular as can be seen in Fig. 1.

Only one quarter of the sample is modeled to reduce the computational cost. The generated mesh consists of uniformly distributed under-integrated hexahedral 8-node solid elements with one integration point. Due to the use of a dynamic code where the Courant condition must be fulfilled, the mesh sizes are limited by computational cost. The element size is around 1.5 mm in the sheets and reduced to 0.1 mm in the vicinity of the nugget, which corresponds to M0.1 in Fig. 3. Although this mesh size does not fully resolve the strain fields in the vicinity of the notch tip, the accuracy of the results are considered valid for the purpose of this work. The resulting mesh has approximately five hundred thousand elements.

An isotropic elasto-plastic constitutive model is applied. J_2 isotropic plasticity is used to describe the yield locus. The gradient of mechanical properties caused by the welding process is modeled through the corresponding hardening curves for each zone. This gradient is correlated with the Vickers' hardness (HV) distribution measured experimentally in the cross section of the welds – as explained in Section 3.1 – and illustrated in Fig. 9 (left). According to Eller *et al.* [26], each hardness value has an associated strain hardening curve (see Fig. 9 right). For FZ, hard HAZ (HHAZ), and BM (showing constant hardness values), the hardening curve corresponding to 497 HV 0.1 is used (blue curve in Fig. 9 right). For the softened HZ or SHAZ (showing a non-uniform hardness distribution) the corresponding stress-strain curve at each Gauss point is obtained by interpolation of the curves in Fig. 9 right [26].
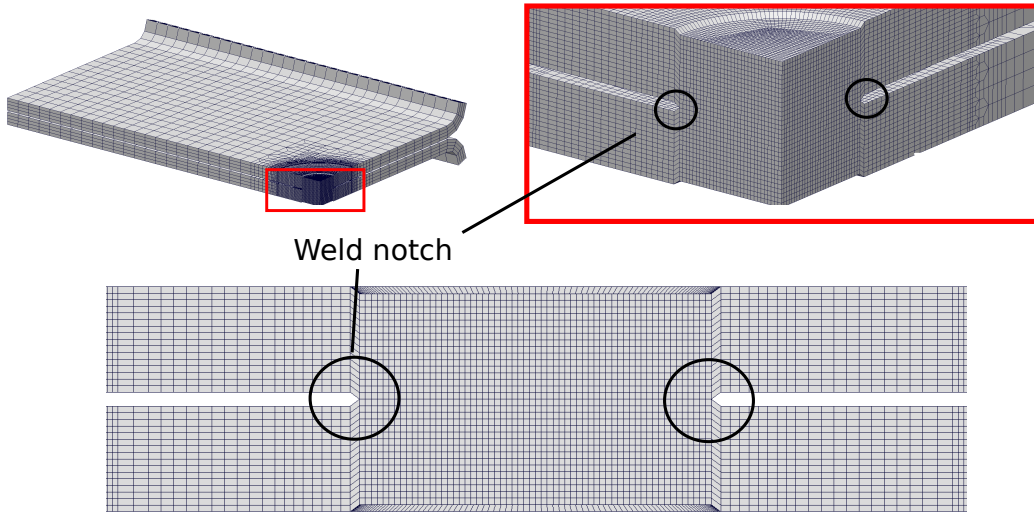
7

Figure 4: Mesh of the loading specimen and the spot weld model. From top left to bottom right: Quarter model of the specimen, zoom in the spot weld zone and detail of the mesh in a front view of the cross sectioned specimen.

The hardness distribution is introduced axisymmetrically, using the dimensions obtained from the hardness profiles presented in Fig. 9. The multiple radii defining the size of the zones (i.e. r_1, r_2 and r_3 in Fig. 9) are obtained from direct measurements of the weld nuggets.

It must be noticed that due to the low loading velocities in the experimental tests (see Section 2.2.2), the problem is treated as a quasi-static one. Since VPS is a dynamic code, a constant low acceleration is introduced as boundary condition in the model, so that the acceleration term becomes negligible and the simulations are not polluted by spurious waves.

2.1.2. J-integral fracture criterion

Experimental evidence has shown that for most of the loading conditions, martensitic steels joints fail due to cracks nucleating at the weld notch tip and propagating through the nugget [14]. Following Dancette *et al.* [5], the J-integral is used to evaluate the intensity of the crack tip stress field. When it reaches a critical value, which is a material property related to the material fracture toughness, a crack nucleates and the joint is assumed to have failed. The J-integral is defined in a two dimensional elastic cracked body as [27]:
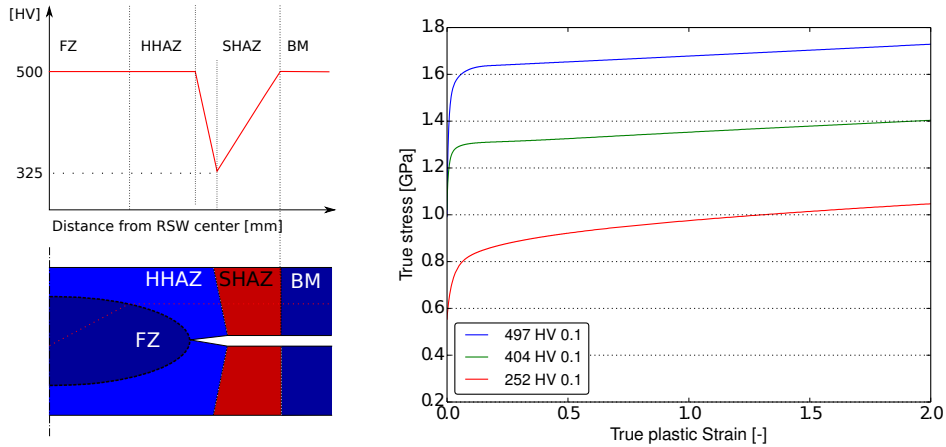
8

Figure 5: On the left, illustrative hardness profile and the associated cross sectioned 22MnB5 spot weld with welding zones. On the right, experimentally measured stress-strain curves for a 22MnB5 steel with different hardness values.

$$J_1 = \int_\Gamma \left[W n_1 - \sigma_{ij} \frac{\partial u_i}{\partial x_1} n_j \right] ds, \tag{1}$$

where Γ is a path beginning at the bottom crack face and ending on the top face (see Fig. 6), $\boldsymbol{n}$ is the outward normal to Γ, $\boldsymbol{\sigma}$ the stress tensor, u the local displacement, and ds the increment of arc length along Γ. W is the strain energy density and is defined as:

$$W = W^e = \int_0^{\boldsymbol{\varepsilon}} \sigma_{ij} d\varepsilon_{ij}^e = \int_0^t \sigma_{ij} \frac{d\varepsilon_{ij}^e}{dt} dt, \tag{2}$$

where ε_{ij}^e are the components of the elastic strain tensor. The concept of J-integral has been extended recently to elasto-plastic materials in accordance with incremental theory of plasticity [28, 29]. In the absence of unloading, as is the case here, path-independent results for the elastic-plastic J-integral can be achieved by selecting an evaluation path Γ enclosing the plastic zone completely [29].

In this paper, the J-integral is evaluated using the equivalent domain integral method [30–32], gathering the strain, stress, and displacement fields from the finite element simulations. The subindices in Eq. 1 refer to the local crack-tip coordinate system (see Fig. 6), with the x_1-axis parallel to the crack propagation direction (see Fig. 7). In this paper, the first crack propagation direction is obtained from the acoustic tensor following Xue *et al.* [33].

9

The J-integral must be evaluated at the weld section at which the stress/strain concentration is critical, i.e. at the point of the weld notch front at which crack propagates first. For the loading angles and the specimen geometry used in this work, previous simulations have shown that this critical section is AA for shear and mixed-mode loading cases, and BB for normal tensions tests (see Fig. 8).
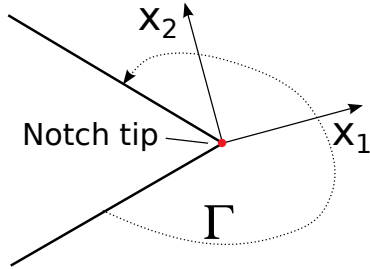

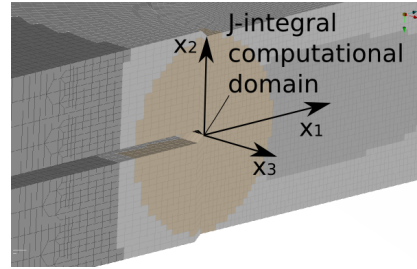Figure 6: Crack tip coordinate system in 2D.

Figure 7: Weld notch zone at which J-integral is evaluated.

Finally, the computed J-integral values are compared with critical values related with the nugget fracture toughness. These values have been obtained from the literature. In the case of shear tests where the crack propagation from the weld notch is related to mode II fracture, a critical value of $J_{IIC} = 56\,\mathrm{kJ\,m^{-2}}$ is assumed [4]. In the case of normal tests, related with mode I fracture, a lower value of the critical J-integral ($J_{IC} = 22.5\,\mathrm{kJ\,m^{-2}}$) is used [3]. Although these critical values correspond to spot welds in a different high strength steel (TRIP780), they can be safely used for 22MnB5 since both steels exhibit a martensitic microstructure with similar hardness and thus similar nugget fracture toughness (see Fig. 10 of [34] and [35]). The critical J-integral values for 22MnB5 weld nugget material have not been found in the literature. It must be noticed that J-integral approach can be used in this work because the spot weld notch is sharp and exhibits a pre-crack ahead of it, as observed in Fig. 1.

2.1.3. Loading conditions

Three type of loading test are simulated, namely normal, shear and mixed-mode tests (see Fig. 8). Displacement are prevented in nodes along the end of the flanges of the bottom sheet of the specimen (red lines in Fig. 8(a)), while a non-zero displacement is applied along the same lines on

the top sheet (blue lines in Fig. 8(a)). The specimens are rotated to represent the three loading modes. In the case of mixed-mode tests, lateral displacements are observed in the DIC measurements of the experiments. These lateral displacements are also introduced as boundary conditions to accurately reproduce the actual test conditions.
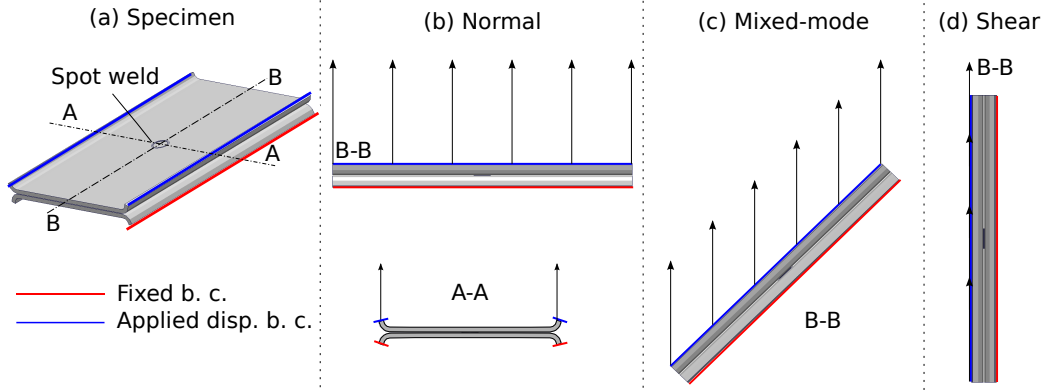

Figure 8: (a) Schematic of the applied displacement boundary conditions, and (b), (c), (d) section of the specimens under normal, mixed-mode and shear loading conditions, respectively.

2.2. Experimental campaign

Two types of experiments are carried out. In a first set of characterization experiments, the values for the model parameters, namely the nugget geometry and the material hardness distribution, are independently measured. The measured material hardness is then correlated with the corresponding strain hardening curves depending on the weld zone as explained in Section 2.1.1 (see Fig. 5). A second set of validation experiments consist in loading tests to obtain the bearing capacity of the joints for the different configurations defined in the test matrix.

The 22MnB5 test sheets are supplied with an aluminum-silicon coating that protects this material against oxidation and decarburization during the hot forming process [36]. In as-delivered state, this steel features a ferritic/pearlitic ductile microstructure, and during the press hardening process and quenching in cooled stamping tools, the microstructure is transformed to a fully martensitic brittle and high strength microstructure (reaching an ultimate tensile strength of 1500 MPa) [36]. The chemical composition of 22MnB5 steel can be seen in Table 1.

11

C	Mn	P	S	Si	Al	Ti	B	Ni	Cr	Cu	V
0.221	1.29	0.018	0.001	0.28	0.032	0.039	0.0038	0.013	0.193	0.01	0.005

Table 1: Chemical composition of 22MnB5 used in this work (wt. %) [37].

Three different sheet thicknesses have been considered for both characterization and loading tests: the minimum and maximum thicknesses currently used in the automotive industry for this steel grade, namely 0.8 mm and 2.0 mm, and an intermediate value of 1.5 mm. Joints with all possible combinations of these thicknesses are tested (see Table 2). Furthermore, the influence of spot weld size is analyzed. For this purpose, different spot weld diameters are generated for a given sheet thickness combination by changing the welding parameters. For the sake of reducing the size of the test matrix, multiple weld diameters are tested only for one of the sheet thickness combination, $t_1 = t_2 = 1.5$ mm. Note that the level of control of the welding parameters is low: for a given set of welding parameters, the resulting diameter cannot be repeated with high accuracy. Around 0.1 mm standard deviation in the diameter is obtained among all joints welded with the same conditions, even without considering those specimens with welding imperfections. In addition, the diameters are measured using a caliper gauge on the failed spot welds or using the micrographs of the cross-sectioned failed welds. Notice that the procedures used to measure the diameter introduces errors of around 0.1 mm. Consequently, the weld diameters are represented in Table 2 using the average measurement of all the specimens of the same thickness combination and welding parameters $\pm$ 0.2 mm.

As-delivered plane sheets of 22MnB5 are hot stamped and cut off to obtain the desired geometry and the martensitic microstructure. Finally, the specimens are joined together using the resistance spot welding technique. A NIMAK C-type servo spot weld gun combined with a HWH control system is used for the welding process. All combinations are welded applying 3 kN constant electrode force with 1000 ms and 200 ms as squeeze and hold times, respectively. Two weld pulses are applied, the first one over 200 ms and welding currents of 3.0 kA, and the second one over 400 ms and current from 4.8 kA to 6.2 kA depending on the thickness combinations and the desired nugget size. These welding parameters are chosen in order to avoid splashes, voids in the weld and electrode damage.

Joint code	Thickness (mm) Sheet 1, t_1	Sheet 2, t_2	Equivalent thickness	Average diameter (mm)
0.8_0.8_3.80	0.8	0.8	0.80	3.8 ± 0.2
0.8_1.5_4.30	0.8	1.5	0.94	4.3 ± 0.2
0.8_2.0_4.00	0.8	2.0	1.04	4.0 ± 0.2
1.5_1.5_5.00	1.5	1.5	1.50	$5.0 \pm 0.2^*$
1.5_2.0_6.20	1.5	2.0	1.60	6.2 ± 0.2
2.0_2.0_5.90	2.0	2.0	2.00	5.9 ± 0.2

Table 2: Sheet thickness combinations and resulting average spot weld diameters measured at the faying surface. The equivalent thickness (t_{eq}) is calculated $t_{eq} = 0.2\ t_M + 0.8\ t_m$, where t_M and t_m are the maximum and minimum thicknesses respectively. *The combination 1.5_1.5_5.00 is welded with multiple welding parameters, 4.00 mm and 6.00 mm joint weld diameters are obtained as well.

2.2.1. Characterization of model parameters

Three specimen for each thickness combination are sacrificed and cross-sectioned in order to determine the material and geometrical parameters for the spot weld model. The Vickers' hardness distribution is measured using an indentation point line crossing all spot weld zones (see Fig. 9) to identify the material zones and their dimensions. Microstructure observations using optical microscope are carried out in order to explain the hardness and local material property distribution.

The specimens that are loaded up to fracture (following the procedure described in Section 2.2.2), are also cross-sectioned after testing in order to measure the weld dimension, examine the fracture surface and identify the failure mechanisms. Micro computed tomography (micro CT) of one interrupted normal test is done as well, to analyze the first crack propagation path steps.

2.2.2. Loading tests

A specimen similar to the KS-II specimen [38] consisting in two welded U-profiles is used to load the joints at different angles between the applied force direction and the sheets' plane, as depicted in Fig. 8. Ninety degrees represents pure normal load mode, zero degrees represents pure shear loading mode, and forty-five degrees angle corresponds to the mixed-mode loading. The tests using specimens of same thickness combination and different weld

sizes are only performed at shear and normal loading. The number of performed tests for each configuration is presented in Table 3.

The joined specimens are loaded using a Zwick Machine equipped with a 250 kN load cell. A device specially designed for this purpose is used to apply the force at the different loading angles. The applied cross-head speeds are 10 mm/min for normal tests, 5 mm/min for mixed-mode tests and 2 mm/min for shear tests. The displacements of both sides of the specimens are measured using Digital Image Correlation (DIC) during the tests.

Sheet thickness combination	Diameter	Loading mode		
		Shear tests	Mixed-mode tests	Normal tests
0.8 - 0.8	3.8	5	5	5
0.8 - 1.5	4.3	5	5	5
0.8 - 2.0	4.0	5	5	5
1.5 - 1.5	4.0	3	0	3
	5.0	3	0	3
	6.0	5	5	5
1.5 - 2.0	6.2	5	5	5
2.0 - 2.0	5.9	5	0	5

Table 3: Number of experimental loading tests for each sheet thickness combination, weld diameter and loading mode. All dimensional magnitudes are given in mm.

3. Results and discussion

3.1. Geometry and microstructure

A typical spot weld cross section of a martensitic steel is represented in Fig. 1, including the different welding zones. Apart from the well-known FZ, HAZ, and BM, HAZ is commonly sub-divided in martensitic steels into three regions based on the peak temperature during welding process [13, 39–41]: upper-critical HAZ (UCHAZ) with peak temperatures above A_{c3}, intercritical HAZ (ICHAZ) where temperature are ranging between A_{c1} and A_{c3}, and sub-critrical HAZ (SCHAZ) with temperatures bellow A_{c1}. In the present work, the HAZ is divided based on the mechanical properties, i.e. the hardening curves shown in Fig. 5, into the hard HAZ (HHAZ) that corresponds to UCHAZ, and the SHAZ that corresponds to both ICHAZ and SCHAZ.

14

The corresponding hardness profile can be seen in Fig. 9, where the different welding zones have been clearly identified. BM, HHAZ and FZ have high hardness values due to their martensitic microstructure. For FZ and HHAZ, martensite is generated during the welding process due to the high cooling rates that these zones undergo. The BM features a fully martensitic microstructure due to the hot forming manufacturing process. The SHAZ features different hardening grades ranging from low to high strength values, due to the various microstructures generated by the different temperature-time histories during welding. The softening in the ICHAZ is promoted by the formation of ferrite-martensite dual phase and the softening in the SC-HAZ is the caused by martensite tempering [13, 39–41].
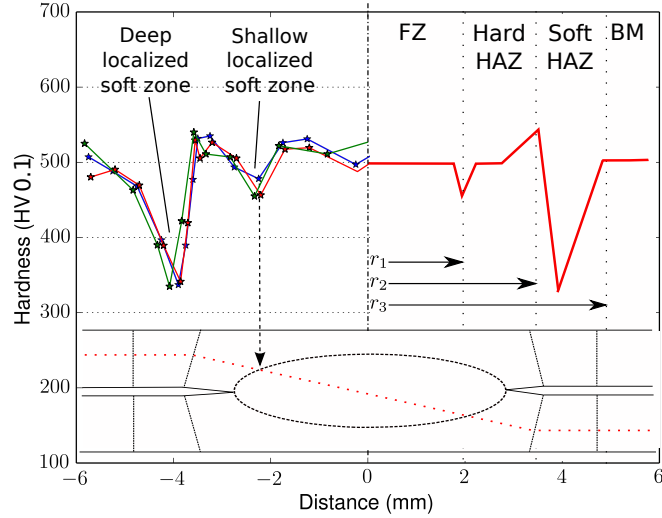
Figure 9: Hardness distribution of martensitic boron steels resistance spot weld, showing the measurement points on the top left and a scheme of the hardness profile with the corresponding zones on the top right.

For all the analyzed sheet thickness combinations, the hardness profiles and values are similar. The only difference is the dimensions of the different zones, represented by the radii shown at the right of Fig. 9, r_1, r_2, r_3. These radii define the size of the different zones and depend linearly on the spot weld size. In addition, an extremely confined and small soft zone is also observed at the boundary between FZ and HAZ, already reported in previous works [42]. This zone constitutes a weaker area.

Apart from the material properties, some geometrical features are ex-

tracted from the cross sections. The weld notch shape is irregular due to the presence of AlSi remains from the sheet coating as observed in Fig. 1. In some cases, there are voids in the nugget due to an incorrect solidification process during welding.

3.2. Experimental loading curves

The force-displacement curves of the shear tests are presented in Fig. 10(a). An illustrative test curve is plotted for each one of the multiple thickness combinations. At first glance, a strong dependency of the maximum forces on the thickness combination is apparent. However, it is observed in Fig. 10(b), where the results of three tests with three different weld sizes are plotted, that the maximum force is extremely sensitive to the spot weld diameter. Moreover, despite the different thickness combination, those joints with similar weld diameter have roughly the same bearing capacity as can be seen for combinations 0.8_1.5_4.30 and 0.8_2.0_4.00 in Fig. 10(b). Consequently, the variation of the maximum forces in Fig. 10(a) derives mainly from the differences in spot weld diameter obtained for each thickness combination. It must be noticed also in Fig. 10(b) that apart from the variation in the loading slopes which are attributed to slight variations in the clamping conditions, the maximum forces are repeatable for joints welded using the same process conditions. It is important to note that all joints with apparent imperfections (such as big nugget voids and welding expulsions) have been discarded.

Fig. 11(a) presents the experimental force-displacement curves of the normal tests. An illustrative curve is presented for each sheet thickness combination. Larger displacements are measured as compared to shear tests due to the bending of the sheets surrounding the weld. This sheet bending depends on the sheet thickness leading to multiple slopes in the curves. A rather weak sensitivity of the maximum forces to the weld diameter is found in Fig. 11(b), while the sensitivity to the thickness combination is apparent. The repeatability of the curves is lower than in the normal tests as observed in Fig. 11(b), mainly after the onset of crack propagation (as presented in Section 3.3).

The results for mixed-mode loading are presented in Fig. 12. Notice that a combination of the observed phenomena for the pure normal and shear test is found here. Higher displacements are observed due to the component of the displacement normal to the shear plane. In addition, due to the applied shear displacement component, a significant influence of the spot weld diameter is observed as in the shear tests case.

16
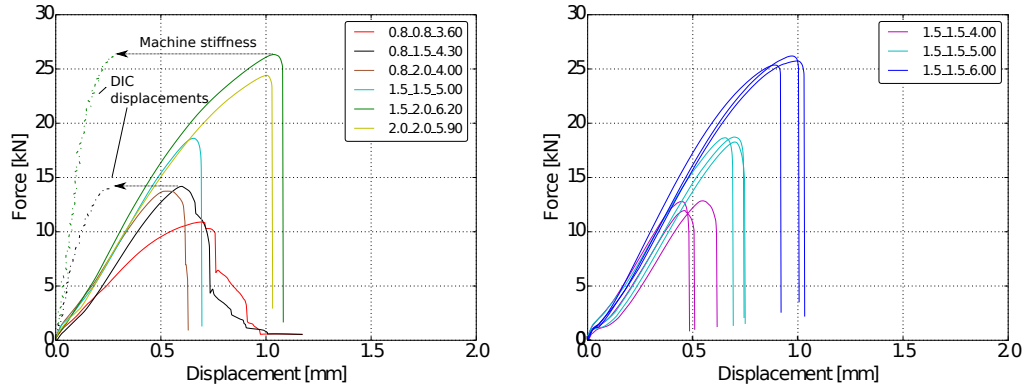
(a) Shear tests results for different sheet thickness combinations.

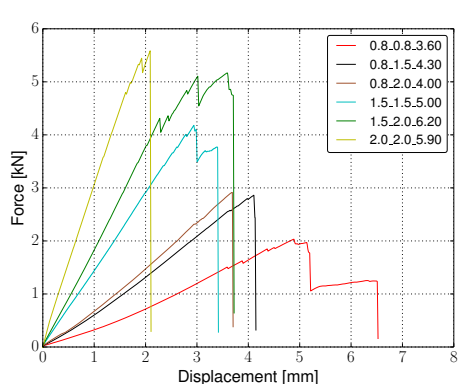(b) Shear tests results for different weld diameters in joints of 1.5 mm sheets.

Figure 10: Experimental force-displacement curves of shear tests. It must be noticed that the actual displacements, measured by DIC, are lower than those measured by the traverse of the tensile machine. The sample codes are given in Table 2.

### 3.3. Spot weld fracture analysis

Upon inspection of the force-displacement curves and the fractured surfaces, two fracture mechanisms are identified in the tested welds: (i) brittle fracture through the nugget or along the nugget boundary in shear and mixed-mode tests, and (ii) ductile fracture of the nugget in normal tests.

Unstable crack propagation splitting the nugget into two pieces after the onset of the crack is observed in shear tests leading to brittle mode II failure of the joint. A brittle fracture surface is observed after failure and the force-displacement curves of the tests drops to zero abruptly after crack nucleation (see Fig. 10). The same behavior is observed in the mixed-mode tests, consistent with the brittle force-displacement curves and the brittle failure surfaces. The shear component of the applied displacements is predominant at this loading angle leading to mode II brittle failure.

In the case of normal tests, the crack advance is stable. Thus, after crack nucleation, higher forces have to be applied to propagate the crack through the material. The crack exhibits a complex three dimensional advance pattern (see Fig. 13), following the weakest path in the FZ material. This path depends on the specific FZ imperfections, leading to low repeatability in the final appearance of the failed spot weld. In some cases, the crack crosses the fusion zone completely and in other cases it turns and advances towards the outer surface of one of the sheets (see Fig. 14). As a result, a large dispersion

17

(a) Normal tests results for different sheet thickness combinations.
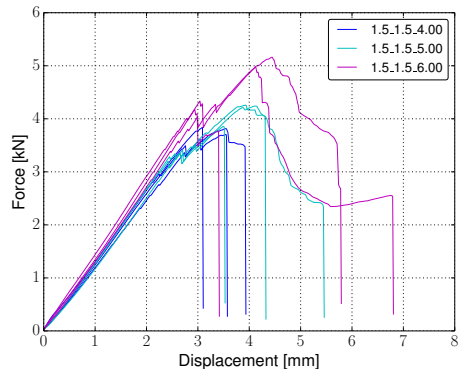
(b) Normal tests results in joints of 1.5 mm sheets for different weld diameters of 4.00, 5.00 and 6.00 mm, respectively.

Figure 11: Experimental force-displacement curves of normal tests. The displacement measured by the machine traverse are considered valid in this case. The sample codes are given in Table 2.

is obtained in the force-displacement curves after crack nucleation. From the industrial point of view, the crack evolution is not relevant since the joint is considered to have failed after the crack nucleation signaled by the first force drop in the force-displacement curve (see Fig. 14).

As presented in Fig. 15, independently from the local fracture mechanism, the crack front propagation after the crack nucleation determines the final appearance of the failed spot welds and the spot welds failure mode introduced in Fig. 2: (i) fracture that crosses the nugget leads to Partial or Full Interface Failure (PIF-FIF), and (ii) fracture along the nugget boundary leads to Partial or Total Dome Fracture mode (PDF-TDF). The crack propagation path is influenced mainly by two factors, the difference in thickness and the loading mode. In most cases, the crack tends to follow the faying surface leading to FIF and PIF failure mode. However, when one of the sheets is much thinner than the other, the predominant crack propagation direction, i.e. that parallel to the sheets plane, is close to the tangent of the fusion zone boundary. In these cases, the crack follows the shallow localized soft zone that is observed in the nugget boundary (see Fig. 9 and [42]), leading to PDF or TDF failure mode (see top pictures in Fig. 15).

The observed failure modes for each thickness combination and loading angle can be seen in Table 4. Each loading mode and sheet combination
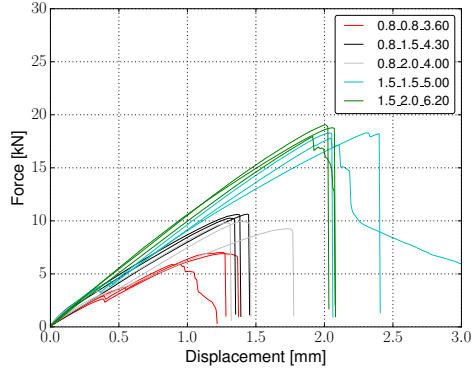
Figure 12: Experimental force-displacement curves in mixed-mode tests. The sample codes are given in Table 2.

does not always fail under the same mode. Despite the fact that the final geometrical appearance of the failed joints is different, the global load at the onset of crack propagation is robust (see e.g. Fig. 14 and Fig. 15). The only difference is in the propagation path.

Code	t1_t2_d	Shear	Mixed-mode	Normal
A	0.8_0.8_3.60	FIF (1) - PDF (4)	FIF (3) - PDF (2)	PIF - PDF (5) *
B	0.8_1.5_4.30	PDF (5)	PDF (5)	PDF (5)
C	0.8_2.0_4.00	PDF (2) - TDF (2)	PDF (4) - TDF (1)	PDF (5)
D	1.5_1.5_4.00	FIF (3)	Not tested	PIF (1) - FIF (2)
E	1.5_1.5_5.00	FIF (3)	Not tested	PIF (1) - FIF (2)
F	1.5_1.5_6.00	FIF (5)	FIF (5)	PIF (4) - FIF (1)
G	1.5_2.0_6.20	FIF (5)	FIF (5)	PIF (4) - FIF (1)
H	2.0_2.0_5.90	FIF (5)	Not tested	FIF (5)

Table 4: Failure modes for each thickness combination, weld diameter and loading mode of 22MnB5 joints. The sample codes are given in Table 2. The numbers in brackets indicate the quantity of tests of each failure mode. *The five tests of combination 0.8_0.8_3.60 fail in a mix of PIF and PDF modes.

3.4. Qualitative validation of loading force-displacement curves up to the onset of crack propagation

The simulated force-displacement curves for the shear tests up to the maximum force exhibits good agreement with the experimental tests results as
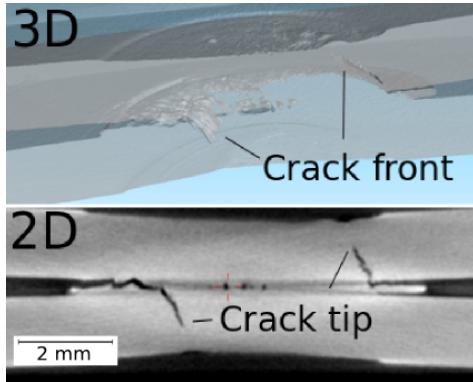
19

Figure 13: Micro CT photo of cross sectioned weld of an interrupted normal test. 3D crack advance is observed.
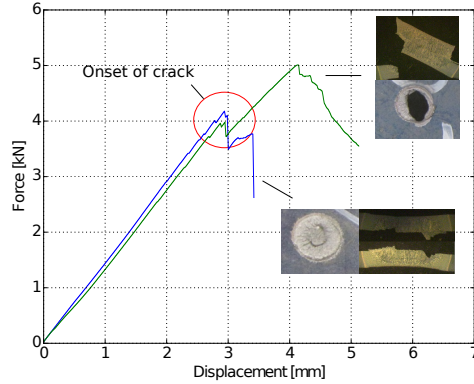

Figure 14: Force-displacement curves depending on crack path.

shown in Fig. 16(a). Notice that the imposed displacements used as boundary condition in the simulations are those measured by the DIC at the specimen, and not those measured by the machine traverse, in order to filter out the machine deformation. The first crack propagation direction obtained using the acoustic tensor approach [33] is the faying surface direction for these cases, i.e. the crack propagates parallel to the sheets' plane. This direction leads to FIF/PIF as observed experimentally in the shear tests (see Table 4). The J-integral is evaluated using this direction as the x_1 axis following the scheme of Fig. 6. The J-integral evolution is plotted against the applied force for different spot weld diameters and sheet thickness combinations, and compared with the critical value for mode II ($J_{IIC} = 56\,\mathrm{kJ\,m}^{-2}$) to obtain the joints maximum forces as presented in Fig. 16(b). It must be noticed that the J-integral-force curves are steep after some point, leading to a low sensitivity of the joint maximum force (bearing capacity) to this critical value of the J-integral. On the other hand, a strong dependence of the J-integral to weld diameter is apparent by comparing the J-integral curves for 1.5_1.5_4.00 and 1.5_1.5_6.00 joints.

Both the experimental and simulated force-displacement curves corresponding to the normal tests of two sheet thickness combinations are presented in Fig. 17(a). Worse agreement between the experimental and simulated results than in shear tests is observed for both small and large thickness combinations. This discrepancy is found mainly in the slope of the curves and is attributed to lack of accuracy in the boundary conditions for the simu-
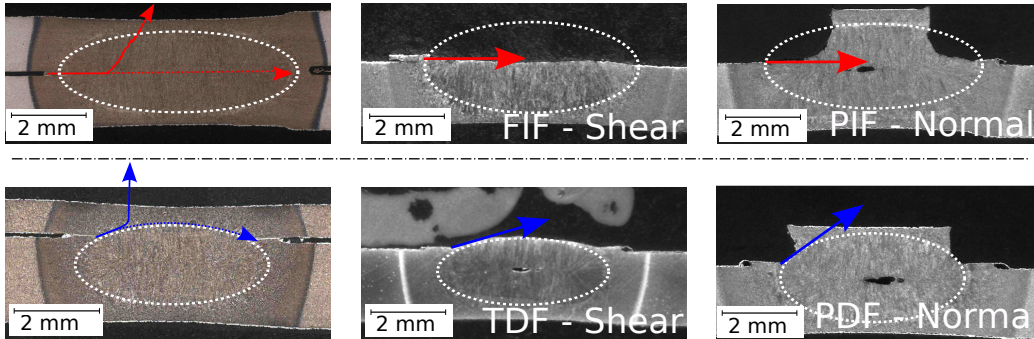
20

Figure 15: Different failure types and zones that can be found in a AHSS spot weld. The left pictures show the two observed crack propagation paths. The arrows on center an right figures indicate the first crack propagation direction. The top pictures show failure starting from the weld notch and crossing completely (leading to FIF as in the center figure) or partially (leading to PIF as in the right figure) the nugget. The bottom pictures indicate failure starting from the notch and surrounding the fusion zone, typically observed in joints with very different thickness. The failure may occur in the complete nugget boundary (leading to TDF as in center figure) or only close to the weld notch with a crack kink (leading to PDF as in right figure).

lations resulting from uncertainties in the experimental setup. The evolution of the J-integral over force is presented in Fig. 17(b) for normal tests of multiple joints. It can be noticed, that the curves are not so sensitive to the weld diameter while the thickness combination has a stronger influence. This phenomenon is explained taking into account the different bending angles produced in the sheets that surround the weld depending on the sheet thicknesses. The J-integral-force curves are not as steep as in the shear tests case. For this reason, the calculated critical forces present higher sensitivity to the critical J-integral value.

Similar results are obtained for mixed-mode tests. Both experimental and simulated force-displacement curves are presented in Fig. 18(a), exhibiting good agreement up to maximum forces where they diverge due to inaccurate boundary conditions representation caused by the bending of the sheets, as in the normal tests case. The crack propagation direction resulting from the acoustic tensor calculation is the faying surface parallel to the sheets' plane. The J-integral evolution using this direction is presented in Fig. 18(b). Due to the combination of the effects of normal and shear conditions, a significant sensitivity to thickness combination and weld diameter is observed. In addition, the applied shear displacements component in this kind of tests

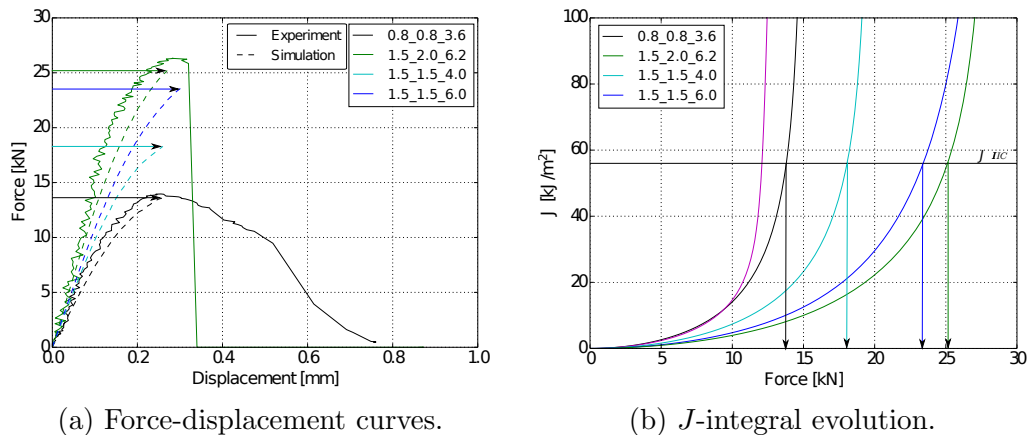(a) Force-displacement curves.   (b) J-integral evolution.

Figure 16: Experimental and simulation results of shear tests. Notice that the scattering in experimental displacements derives from the DIC measurements. The sample codes are given in Table 2.

produces higher stress concentration than the normal component and consequently, the same critical J-integral value of mode II fracture is used ($J_{IIC} = 56\,\mathrm{kJ\,m^{-2}}$).

3.5. Quantitative validation of bearing capacity

The maximum forces obtained from the experimental tests are compared quantitatively in Fig. 19 with those estimated from FE simulations according to the proposed J-integral based procedure.

The results of the shear tests are presented in Fig. 19(a). Strong agreement is observed between experimental and simulated result, with a maximum error of 14 %. The small discrepancies are partly attributed to errors in the spot weld diameter measurements. The maximum forces are plotted versus the measured spot weld diameters in Fig. 20, indeed revealing a strong sensitivity of the maximum forces to the weld size.

Normal tests results are presented in Fig. 19(b). The force at the onset of crack propagation, which is identified by the first significant force drop in the force-displacement curves, is used as the experimental critical force (see Fig. 14). The simulation-based estimates follow the trend of the experimental forces with an underestimation for all cases. Notice that in these tests, higher scatter in the maximum forces of the experimental results are observed. This phenomenon is mainly a consequence of the irregularities in the geometry of the weld notch that determines the first crack nucleation during mode I load-

22

(a) Force-displacement curves.
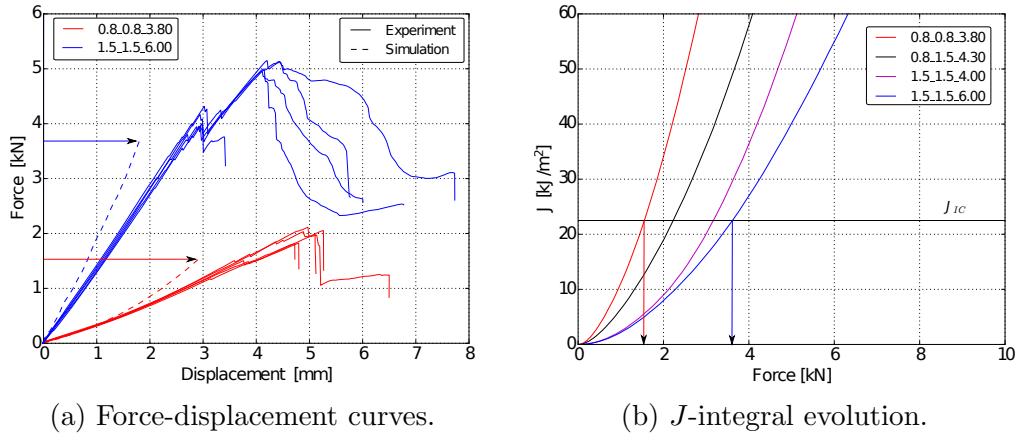(b) J-integral evolution.

Figure 17: Experimental and simulation results of normal tests. The sample codes are given in Table 2.

ing (see Fig. 1). The underestimation is partially attributed to the low value of the critical J-integral for mode I ($J_{IC} = 22.5\,\mathrm{kJ\,m^{-2}}$) used in this work, which has been obtained from the literature. This value could be measured more precisely for the nugget material using independent experimental tests. However, such a characterization is out of the scope of this work.

Finally, the mixed-mode tests results are presented in Fig. 19(c), exhibiting good agreement between simulation and experiments, the maximum error between the experimental and simulated forces is of 8 % in combination 0.8_0.8_3.80. As discussed previously, the fracture mode in the mixed-mode loading tests is close to that in the shear tests. The applied tangential displacement component of these tests leads also to strong sensitivity to weld diameters as in the shear tests. The small discrepancies in the maximum forces can be therefore attributed to the errors in the spot weld diameter measurements.

The simulated estimates for all presented combinations are plotted in Fig. 19(d). It is observed that higher maximum forces are attained in the shear tests. The results of mixed-mode tests are closer to shear tests, due to the higher relevance of the shear component. Increasing maximum forces with the equivalent thickness (see Table 2) is observed for all tests. However, the rate of increasing strength is different depending on the loading angle. To illustrate it, the maximum forces are plotted over the spot weld diameter in Fig. 20 for different loading cases and thickness combinations. On the one hand, for the shear tests, the variation of the maximum forces results from
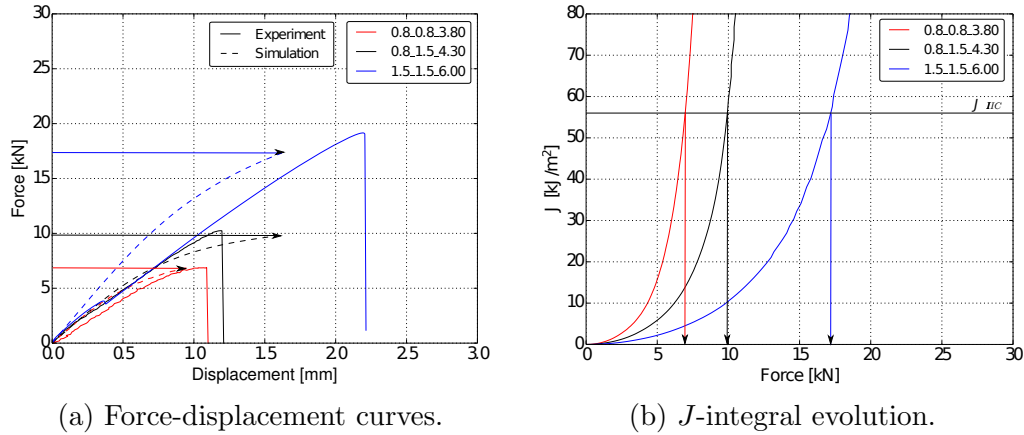
(a) Force-displacement curves.　　　　(b) J-integral evolution.

Figure 18: Experimental and simulation results of mixed-mode tests. The sample codes are given in Table 2.

4. Conclusions

A computational model to estimate the bearing capacity of resistance spot welds for a martensitic boron steel, 22MnB5, was developed in this paper. The model has been thoroughly validated against experiment considering multiple combinations of sheet thickness, weld sizes and loading modes.

Although multiple fracture patterns are observed experimentally in the failed spot welds, fracture is always initiated by stress concentrations at the weld notch leading to crack propagation, and joint failure. Consequently, a non-local J-integral based criterion can be used to determine the onset of fracture, which is assimilated here to joint failure. The J-integral is computed ahead the weld notch and compared with a critical value related with the martensitic nugget fracture toughness. The J-integral critical value depends also on the fracture mode (J_{IC} for mode I and J_{IIC} for mode II). In the case of mixed-mode loading, the shear component is predominant and J_{IIC} values were used for the evaluation of maximum forces. Although the critical J-integral values where obtained from a steel with different composition (TRIP
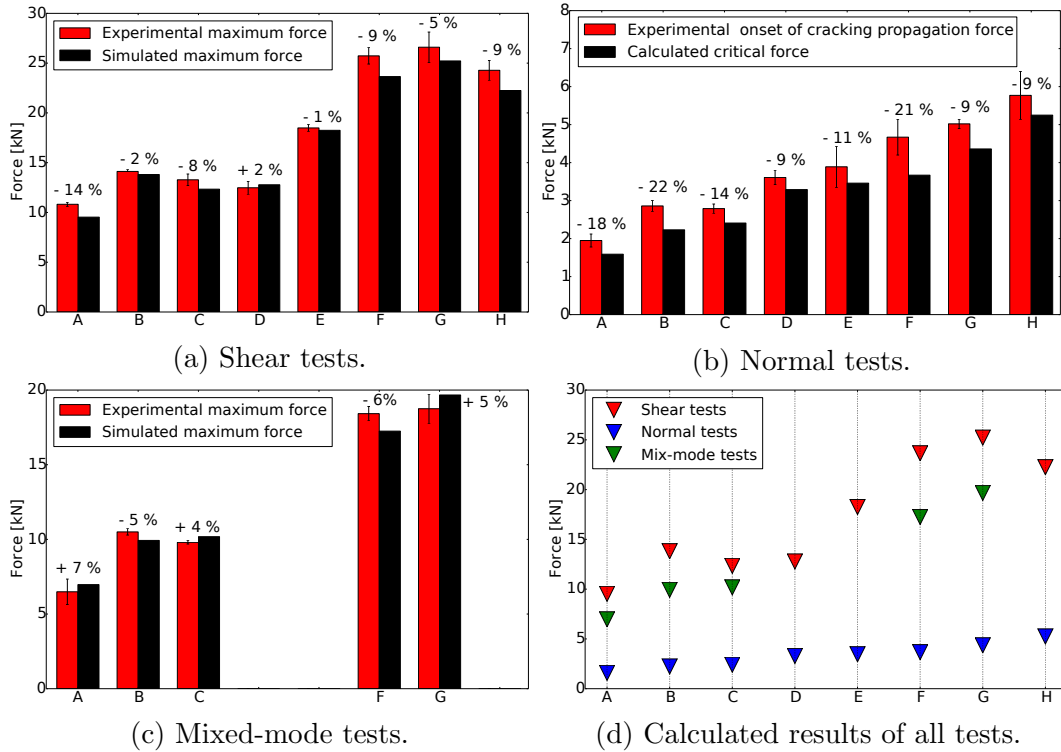
Figure 19: Simulated and experimental critical forces are plotted here for each thickness combination and corresponding diameter. Error bars represent the standard deviation in the experimental results of the tests of each weld configuration. The numbers on top indicate the percentage difference between experimental and simulated results. The sample codes are presented in Table 4.

780), and important factors such as lath and block size of the martensite and the segregation patterns in the nugget have been neglected, very good agreement has been obtained between experimental and simulation results, especially in the case of load tests dominated by mode II.

The main observed differences between calculated and experimental results are attributed to uncertainties in the geometry and the presence of local imperfections (voids or welding splashes) that may reduce the joint bearing capacity and introduce scattering in the results not reproducible with a flawless FE model. More accurate measurements of the spot weld size, alongside a better characterization of the critical J-integral, an analysis of the influence of the spot weld imperfections, and account for residual stresses originated by the welding process, would further improve the agreement between exper-
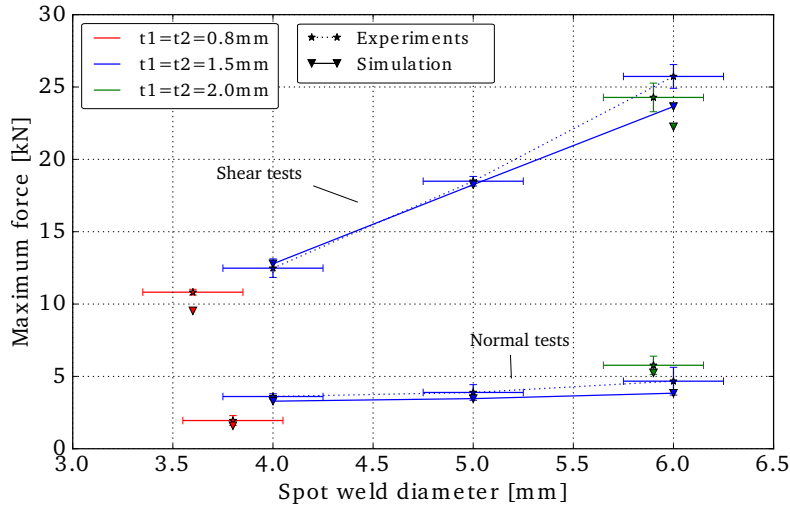
Figure 20: Experimental and simulated maximum forces are plotted versus the weld diameter. The experimental forces are plotted with error bars representing the standard deviation of the test repetitions. Welding diameters are plotted with error bars considering the measurement errors of $0.2 \pm$ mm. The colors indicate the different thickness combinations.

iment and model predictions and are all currently under consideration. The extension of the methodology for different AHSS grade and for dissimilar joints is under development.

Acknowledgement

[1] C. M. Tamarelli. AHSS 101 the evolving use of advance high-strength steel for automotive applications. Technical report, Steel Market Development Institute, Southfield, 2011.

[2] S. Keeler and M. Kimchi. *Advanced high strength steels for automotive industry*. Number 2. WorldAutoSteel, 2014.

[3] S. Dancette, D. Fabrègue, V. Massardier, J. Merlin, T. Dupuy, and M. Bouzekri. Experimental and modeling investigation of the failure resistance of Advanced High Strength Steels spot welds. *Engineering Fracture Mechanics*, 78(10):2259–2272, 2011.

[4] S. Dancette, D. Fabrègue, V. Massardier, J. Merlin, T. Dupuy, and M. Bouzekri. Investigation of the Tensile Shear fracture of Advanced High Strength Steel spot welds. *Eng. Fail. Anal.*, 25:112–122, 2012.

[5] S. Dancette, D. Fabrègue, R. Estevez, V. Massardier, T. Dupuy, and M. Bouzekri. A finite element model for the prediction of Advanced High Strength Steel spot welds fracture. *Engineering Fracture Mechanics*, 87:48–61, 2012.

[6] T. K. Eller, L. Greve, M. T. Andres, M. Medricky, and V. T. Meinders. The softened heat-affected zone in resistance spot welded tailor hardened boron steel: a material model for crash simulation. In *International Conference of Impact Loading of Structures and Materials*, pages 3–6, 2016.

[7] M. Pouranvari and S. P. H. Marashi. Critical review of automotive steels spot welding: process, structure and properties. *Science and Technology of Welding and Joining*, 18(5):361–403, 2013.

[8] T. Huin, S. Dancette, D. Fabrègue, and T. Dupuy. Investigation of the Failure of Advanced High Strength Steels Heterogeneous Spot Welds. *Metals*, 6(5):111, 2016.

[9] V. J. Badheka, S. K. Agrawal, and N. Shroll. Mode of failure of resistance spot welded martenstic stainless steel-Part II. *International Journal of Mechanical and Materials Engineering*, 5(1):43–52, 2010.

[10] M. Pouranvari, S. P. H. Marashi, and S. M. Mousavizadeh. Failure mode transition and mechanical properties of similar and dissimilar resistance

spot welds of DP600 and low carbon steels. *Science and Technology of Welding and Joining*, 15(7):625–631, 2010.

[11] M. Pouranvari and S. P. H. Marashi. Failure mode transition in AHSS resistance spot welds. Part I. Controlling factors. *Materials Science and Engineering: A*, 528(29-30):8337–8343, 2011.

[12] M. Pouranvari, S. P. H. Marashi, and D. S. Safanama. Failure mode transition in AHSS resistance spot welds. Part II: Experimental investigation and model validation. *Materials Science and Engineering: A*, 528(29-30):8344–8352, 2011.

[13] M. Pouranvari, S. Sobhani, and F. Goodarzi. Resistance spot welding of MS1200 martensitic advanced high strength steel: Microstructure-properties relationship. *Journal of Manufacturing Processes*, 31:867–874, 2018.

[14] M. Pouranvari. Understanding the factors controlling the interfacial failure strength of advanced high-strength steel resistance spot welds: hardness vs. fracture toughness. *Science and Technology of Welding and Joining*, 1718:1–7, 2018.

[15] Y. J. Chao. Ultimate Strength and Failure Mechanism of Resistance Spot Weld Subjected to Tensile, Shear, or Combined Tensile/Shear Loads. *Journal of Engineering Materials and Technology*, 125(2):125, 2003.

[16] Y. J. Chao. Failure mode of spot welds: interfacial versus pullout. *Science and Technology of Welding and Joining*, 2003.

[17] S.-H. Lin, J. Pan, T. Tyan, and P. Prasad. A general failure criterion for spot welds under combined loading conditions. *International Journal of Solids and Structures*, 40(21):5539–5564, oct 2003.

[18] M. Pouranvari, S. P. H. Marashi, M. Goodarzi, and A. Abedi. An analytical model predicting failure mode of resistance spot welds. In *17th International Conference on Metallurgy and Materials*, volume 13, pages 1–7, Hradec nad Moravicí, 2008.

[19] T. L. Anderson. *Fracture Mechanics: Fundamentals and Applications, Third Edition*. CRC Taylor & Francis, 2005.

[20] S. Sommer. Modeling of the fracture behavior of spot welds using advanced micro-mechanical damage models. In *IOP Conference Series: Materials Science and Engineering*, volume 10, page 012057, 2010.

[21] S. Burget and S. Sommer. Characterization and modeling of fracture behavior of spot welded joints in hot-stamped ultra-high strength steels. In *11. LS-DYNA Forum*, Ulm, 2012.

[22] S. Burget and S. Sommer. Modeling of deformation and failure behavior of dissimilar resistance spot welded joints under shear, axial and combined loading conditions. *ICF13*, pages 1–12, 2013.

[23] A. L. Gurson. Continuum theory of ductile rupture by void nucleation and growth: Part 1-Yield criteria and flow rules for porous ductile media. *Journal of Engineering Materials and Technology, Transactions of the ASME*, 99 Ser H(1):2–15, 1977.

[24] M. Gologanu, J.-B. Leblond, and J. Devaux. Approximate models for ductile metals containing non-spherical voids. Case of axisymmetric prolate ellipsoidal cavities. *Journal of the Mechanics and Physics of Solids*, 41(11):1723–1754, 1993.

[25] A. Pandolfi and M. Ortiz. An eigenerosion approach to brittle fracture. *International Journal for Numerical Methods in Engineering*, 92(June):694–714, 2012.

[26] T. K. Eller, L. Greve, M. T. Andres, M. Medricky, V. T. Meinders, and A. H. van den Boogaard. Determination of strain hardening parameters of tailor hardened boron steel up to high strains using inverse FEM optimization and strain field matching. *Journal of Materials Processing Technology*, 228:43–58, 2016.

[27] J. R. Rice. A Path Independent Integral and the Approximate Analysis of Strain Concentration by Notches and Cracks. *Journal of Applied Mechanics*, 35(2):379, 1968.

[28] N. K. Simha, F. D. Fischer, G. X. Shan, C. R. Chen, and O. Kolednik. J-integral and crack driving force in elastic-plastic materials. *Journal of the Mechanics and Physics of Solids*, 2008.

[29] O. Kolednik, R. Schöngrundner, and F. D. Fischer. A new view on J-integrals in elastic-plastic materials. *International Journal of Fracture*, 187(1):77–107, 2014.

[30] F Z Li, C F Shih, and A Needleman. A comparison of methods for calculating energy release rates. *Eng. Fail. Anal.*, 21(2):405–421, 1985.

[31] G. P. Nikishkov and S. N. Atluri. An equivalent domain integral method for computing crack-tip integral parameters in non-elastic, thermo-mechanical fracture. *Eng. Fract. Mech.*, 26(6):851–867, 1987.

[32] G. P. Nikishkov and S. N. Atluri. Calculation of fracture mechanics parameters for an arbitrary three-dimensional crack, by the "equivalent domain integral" method. *International Journal for Numerical Methods in Engineering*, 24:1801–1821, 1987.

[33] L. Xue and T. Belytschko. Fast methods for determining instabilities of elasticplastic damage models through closed-form expressions. *Int. J. Numer. Methods Eng.*, 84:1490–1518, 2010.

[34] F. Krajcarz, A.-F. Gourgues-Lorenzon, E. Lucas, and A. Pineau. Fracture toughness of the molten zone of resistance spot welds. *International Journal of Fracture*, 181(2):209–226, 2013.

[35] M M Megahed and A M Eleiche. Fracture Toughness Properties of High-Strength Martensitic Steel within a Wide Hardness Range. *J. Mater. Eng. Perform.*, 10(October):576–585, 2001.

[36] ArcelorMittal. Steels for hot stamping, product catalog, 2012.

[37] D. Berglund, K. Amundsson, and L.-Olof Hellgren. Hot stamped components with soft zones - simulation and validation of material properties and product performance. In *International Conference on Hot Sheet Metal Forming of High-Performance Steel*, Kassel, 2008.

[38] O. Hahn, D. Gieske, and A. Rhode. Probe und Probenspannvorrichtung zum Einsatz in Zugmaschinen, 1996.

[39] T. K. Eller. *Modeling of tailor hardened boron steel*. PhD thesis, University of Twente, 2016.

[40] T. K. Eller, L. Greve, M. T. Andres, M. Medricky, A. Hatscher, V. T. Meinders, and A. H. Van Den Boogaard. Plasticity and fracture modeling of the heat-affected zone in resistance spot welded tailor hardened boron steel. *Journal of Materials Processing Technology*, 234(1):309–322, 2016.

[41] M. Tamizi, M. Pouranvari, and M. Movahedi. Welding metallurgy of martensitic advanced high strength steels during resistance spot welding. *Science and Technology of Welding and Joining*, 22(4):327–335, 2017.

[42] O. Sherepenko and S. Jüttner. Schweißtechnische Verarbeitung höchstfester Stähle: Widerstandspunktschweißen unter Berücksichtigung fertigungs- bedingter Spalte, 2013.